



Contents lists available at ScienceDirect

## International Journal of Mechanical Sciences

journal homepage: [www.elsevier.com/locate/ijmecsci](http://www.elsevier.com/locate/ijmecsci)

## Sea sponge-inspired designs enhance mechanical properties of tubular lattices

Ailin Chen<sup>a</sup>, Ukamaka Ezimora<sup>a,b</sup>, Sangryun Lee<sup>a,c</sup>, Jeong-Ho Lee<sup>a</sup>, Grace X. Gu<sup>a,\*</sup><sup>a</sup> Department of Mechanical Engineering, University of California, Berkeley, CA 94720, USA<sup>b</sup> Department of Mechanical Engineering, University of California, Merced, CA 95343, USA<sup>c</sup> Division of Mechanical and Biomedical Engineering, Ewha Womans University, Seoul 03760, South Korea

## ARTICLE INFO

## Keywords:

Bioinspired design  
 Additive manufacturing  
 Buckling analysis  
 Tubular lattice  
 Powder-bed fusion  
 Compression strength

## ABSTRACT

The sea glass sponge, a marine organism with a distinctive tubular lattice skeleton, offers inspiration for developing resilient structures with exceptional buckling resistance. Previous work on sponge lattices focuses on mimicking the diagonal feature of the sponge unit cell; however, current understanding on the effects of the tubular three-dimensional arrangement seen in glass sponges is incomplete. This study seeks to leverage the benefits of sea glass sponge structures to enhance the performance of three-dimensional tubular lattices with improved compressive strength and elastic energy absorption. Through a combination of experimental and simulation techniques, we systematically examine the influence of varying cross-sectional shape and geometry of three-dimensional tubular lattice structures. Our experimental findings reveal that the sponge-inspired pattern surpasses all unit cell designs under compression loads. Sponge designs with a hexagonal cross-section exhibit the highest buckling strength, with a 74.9 % improvement over the non-reinforced design and a 39.0 % improvement within sponge designs. Meanwhile, the sponge designs with a circular cross-section show the best energy absorption, achieving a 90.8 % improvement over the non-reinforced design and a 54.0 % increase within sponge designs. Computational results show this novel design achieves improved stress distribution and stability due to the self-reinforcement of the struts' orientation and reduction of stress concentration at sharp corners, which helps explain these findings. This study motivates the design of sea glass sponge structures for applications such as aerospace, marine, and infrastructure that requires high strength-to-weight ratio and buckling resistance.

## 1. Introduction

Engineers and scientists are captivated by nature's remarkable biological adaptive features, leading to innovative bioinspired structures with advanced properties [1–4]. Such examples include stiff but flexible structures from fish scale [5,6], structures with excellent elastic behavior from bamboo [7,8], mechanically robust composite from nacre [9,10], and reduced noise wing design from owl feather [11]. Recently the elaborate internal skeletal structure of the sea glass sponge has been the subject of interest due to their combination of structural resilience and efficient strength-weight utilization [12–15]. In the skeletal sponge anatomy, there exists a structural hierarchy of three levels. The first being a networked architecture containing helical beams separated by deformable thin organic interlayers. It has been shown in recent literature that these helical beams enhance resilience against collapse [16–20]. The second being a uniform square grid fortified by diagonal

struts that cut across every other cell. The grid-like structure contains two pairs of bisecting diagonal struts creating a symmetric pattern of alternating open and closed cells [21–24]. The last being the nested cylindrical structure called spicule. For each spicule, rings decrease in thickness proceeding radially outward with a solid cylinder in the center [25–27]. Researchers have also studied the moisture effect of the sponge [28,29].

To uncover the underneath mechanism of the sponge inspired structure, literature is divided into two groups where one studies the in-plane properties of the sponge structure and the other studies the out-of-plane performance of the sponge structure. Sharma et al. developed an analytical model from an energy based theorem to formulate the in-plane effective elastic modulus and Poisson's ratio of the sponge structure [30]. Zhang et al. discovered that the sponge-inspired lattice structure experiencing a combination of buckling with layer-by-layer crushing and rotation with uniform crushing when subjected to

\* Corresponding author.

E-mail address: [ggu@berkeley.edu](mailto:ggu@berkeley.edu) (G.X. Gu).<https://doi.org/10.1016/j.ijmecsci.2024.109815>

Received 29 March 2024; Received in revised form 13 October 2024; Accepted 2 November 2024

Available online 3 November 2024

0020-7403/© 2024 Elsevier Ltd. All rights reserved, including those for text and data mining, AI training, and similar technologies.

in-plane compression [31]. Sharma et al. applied cyclic loading to Thermoplastic polyurethane (TPU) printed sponge structure and observed good recoverability with little softening effect in the first cycle [32]. Fernandes et al. compared the sponge lattice with other commonly used lattice structures under static compression and bending, and the sponge lattice had surpassed other designs in all mechanical evaluations [33]. Other than excellent in-plane performance, the sponge design also has high specific energy absorption and high crushing force efficiency under out-of-plane loading conditions, innovating the next generation of lightweight structures with unprecedented mechanical behavior [34, 35]. In addition to above, the sea sponge structure has stimulated creative structures with hydrodynamic benefit [36–38], optical benefit [39,40], super durable properties [41], high performance 3D lattice [42, 43], and tunable soft actuator [44,45].

Previous work on sponge lattices focused on mimicking the diagonal feature of the sponge unit cell. However, current understanding of the effects of the tubular three-dimensional arrangement seen in glass sponges is incomplete. Tubular lattices are well known for their lightweight [46,47] and high structural efficiency features [48–51]. Sharma et al. investigated sponge-inspired thin-tube structures, revealing that bionic tubes fabricated via selective laser melting (SLM) had better fatigue performance and stress distribution compared to honeycomb-based tubes under cyclic loading [52]. Their group found that heat treatment significantly reduced residual stresses and improved fatigue life, though with a decrease in strength due to increased ductility [53]. Sharma et al. also studied the crashworthiness of bio-inspired thin tubes, showing improved energy absorption and reduced peak-to-mean crushing force difference under axial and oblique loads, validated through FEM and experiments [54]. Zhang et al. demonstrated that sponge-inspired tubular structures with circular cross-section exhibited 3–4 times higher strength and toughness compared to traditional designs, with enhanced resistance to axial and radial compression, making them suitable for medical implants and structural applications [55]. These studies highlighted the remarkable potential of sponge-inspired thin-walled structures for improving fatigue performance and energy absorption under cyclic and impact loads. Nonetheless, current research lacks an in-depth investigation into the interaction between cross-sectional geometry and the structural response to buckling behavior.

This study seeks to leverage the benefits of sea glass sponge structures to create three-dimensional tubular lattices with improved compressive strength and elastic energy absorption. Specifically, we examine the influence of cross-sectional shape of sponge inspired tubular lattices on their compression and buckling resistance. A suite of five geometrical shapes is chosen for the cross-sectional designs, while maintaining a constant volume fraction and height. The sea sponge inspired pattern is compared to three other unit-cell patterns which includes an asymmetric diagonally reinforced pattern, a symmetric diagonally reinforced pattern, and a non-diagonally reinforced pattern. All unit cells maintain a constant size of 34 mm by 34 mm. Additive manufacturing and compression experiments are conducted to measure the modulus and buckling strength of the tubular designs. Numerical analyses are also undertaken to complement experimental results and provide a more systematic prediction of mechanical properties. Identifying the superior properties of sea glass sponge tubular lattice will offer novel design guidelines and principles for the development of next-generation buckling resistant structures, advancing the creation of lightweight, impact-resistant protective systems.

The structure of this paper is as follows. Section 2 describes the design inspirations and key variables used in this study, along with the experimental setup, including fabrication and testing, and the simulation methods. In Section 3, we present the experimental and simulation results of the sponge inspired tubular lattices under compression, followed by an analysis of the findings. Finally, Section 4 provides the conclusions drawn from this research.

## 2. Materials and methods

This section elaborates on the procedure to design the bioinspired tubular lattice based on the natural sea sponge. It introduces the control variables and design dimensions, followed by the 3D printing, compression testing, and static simulation setup.

### 2.1. Structural designs

Three key design variables are chosen for this study: cross-sectional geometry, unit cell pattern, and material composition (Fig. 1). Studying cross-sectional geometry can help to identify the buckling model and failure stability of the tubular structure under the influence of cross-sectional shape. It is of note that some geometries, such as circles, have limited potential in making an array of tubular lattices due to their minimal tangential contact. The other two variables can help to provide a fair evaluation of the evolutionary sponge design. By comparing the sponge pattern to other commonly used patterns (shown in Fig. 1c) and varying the material composition, we can better understand the sensitivity of the structural resilience to material attributes. Below, we delve into the rationale behind these chosen variations.

Starting with the cross-sectional geometry, the five different shapes modeled are circular (CIR), triangular (TRI), square (SQR), rectangular (REC), and hexagonal (HEX). All geometries have the same volume of 11,803 mm<sup>3</sup>. These geometries are chosen based on previous findings from literature for variable shape columns [56]. Previous literature has compared square concrete-filled steel tubes (CFST) to circular, square, hexagonal, and octagonal shapes, and found that circular CFST columns exhibit better resistance to local buckling. While comparing squares and polygons, circular columns have better ductility and have higher ultimate strains. Conversely, the square and triangle columns had the smallest strains compared with others [56,57]. Experiments showed rectangular columns to slightly underperform in comparison to square columns [58]. Scarce studies have compared rectangular columns to other shapes, so their behavior is slightly unpredictable. Hexagonal shapes are commonplace in nature, seen in structures such as snowflakes or honeycombs. The hexagonal shape combines the merits of the circular and square cross-sections. Due to there being more vertices in the hexagon shape, there is a better strain energy density distribution [59].

Different unit cell patterns are built and studied, which are the building blocks tessellated along the sides of each geometry. Pattern A is derived from the sea glass sponge. Here, some of the struts cross to form a hexagonal shape which experimental studies have shown to be bending-dominated and more compliant under uniaxial compression. Squares and triangles are also present in Pattern A, which provide more stiffness to the structure [60]. As illustrated in Fig. 1b, Pattern A is defined by several geometric parameters. The variable  $S$  represents half the length of the unit cell. The distance between the diagonal struts (orange beams) and the nearest frame (green beams) is denoted by  $A$ . The width of the unit cell frame (green beams) is labeled  $B_m$ , while  $B_d$  represents the width of the diagonal struts (orange beams). The relationships between these geometric parameters are provided below:

$$A = S / (\sqrt{2} + 2), \quad (1)$$

$$B_m = 0.15 \times S, \quad (2)$$

$$B_d = 0.075 \times S \quad (3)$$

Pattern D is a simple grid with no diagonal reinforcement and has been shown to be weak in resistance to shear forces [61]. Pattern B builds on Pattern D, with the addition of diagonals that span two squares of the unit cell. Pattern C is inspired by cross-braced structures such as those used in civil engineering [33]. The four different unit cells are wrapped around the sides of each cross-sectional shape and given an equal distribution for all but the SQR model. The distributions are as

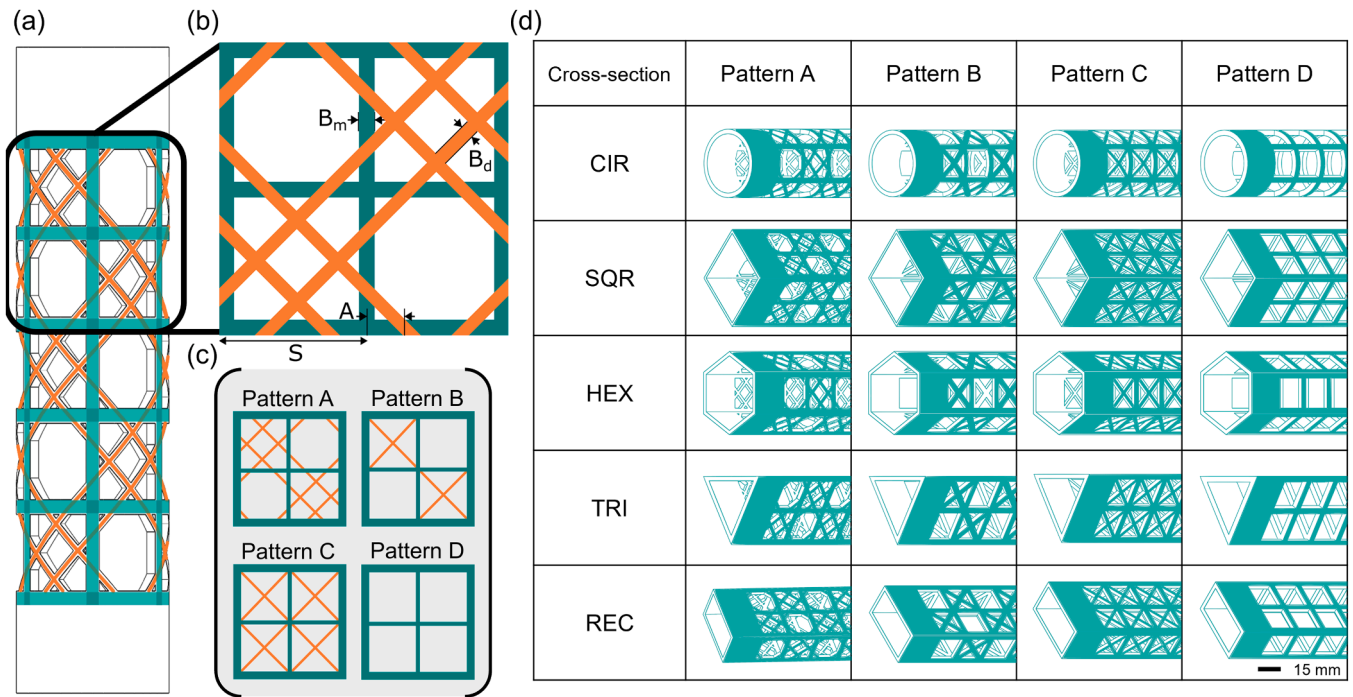


**Fig. 1.** Schematic of design variables. (a) Front view of the tubular lattice design that includes diagonal features that connect with adjacent unit cells. (b) Magnified view of the unit cell using Pattern A as an example. The unit cell has a side length of  $2S$  and non-diagonal elements thickness of  $B_m$  and diagonal elements thickness of  $B_d$ . The diagonal elements in Pattern A have a distance  $A$  from the vertical struts. (c) Schematic of Pattern A-D's unit cell. (d) Cross-section designs for the varying patterns. In total, there are five cross-section designs and four pattern designs.

follows: a  $6 \times 5$  unit cell tessellation for the CIR, TRI, REC, and HEX models and an  $8 \times 5$  tessellation for the SQR models. The dimensions of each design can be found in supplementary information, Table S1.

## 2.2. Specimen fabrication and testing

Additive manufacturing, specifically the multi-jet fusion (MJF) 3D-printing technology, is used to manufacture the various samples [62]. Two commonly used polymers, polyamide 12 (PA12) and polyamide 11 (PA11), are used for this study [63]. PA11 is slightly more ductile than PA12 but the overall mechanical properties are similar [64]. Base material properties for PA12 and PA11 are shown in reference [65,66], and the stress-strain curves of both materials can be found in Supplementary Fig. S1. For consistency purposes, all the samples are printed with the same orientation. The specimens are subjected to uniaxial compression using an Instron 5900-series universal testing system. Three samples are printed and tested for each design. Given the study's focus on the elastic properties of the structure, it is essential to obtain a stress-strain relationship. Therefore, samples are compressed at an extension rate of 5 mm/min until failure in the first trial, or until the highest stress is reached in trials two and three. The compressive load and the displacement of the specimen are obtained from testing, both measured at intervals in time. Then the strain is calculated by normalizing the displacement data from the initial length of the sample. The stress is calculated by dividing the force data from the top surface area of the sample. After obtaining this information, the ultimate strength is calculated from the maximum stress point, and the Young's modulus is calculated by fitting the linear region of the stress-strain data using a linear curve fit. For the modulus of resilience calculation, the area of elastic region is assumed to be a right triangle in which the height is ultimate strength, and the base is the strain at ultimate strength.

## 2.3. Simulation setup

A finite element (FE) simulation is performed using COMSOL to

obtain the stress field distribution for all the candidate designs. In the simulations, 3D models are imported, and a physics-controlled tetrahedral mesh is generated. For the material properties, we adopt a linear elastic model for PA12 [65] with the Poisson's ratio value as 0.43 and the Young's modulus as 1.8 GPa. Due to the similarity of the properties and mechanical behavior of PA12 and PA11, we focus on performing simulations on PA12. During the simulation, a fixed boundary condition is applied to the bottom of the sample, and a displacement of 2 % is applied on the top surface in a downward direction. It is difficult to observe the 2nd or higher buckling mode in experiments due to significantly higher critical loads beyond material limits; therefore, we use the first critical loading factor which is the load factor for first eigenmode for the buckling element. Sensitivity tests (Supplementary Fig. S2) indicate that the simulation results converge at approximately 7000 total elements, which we have adopted as the mesh size.

## 3. Results and discussion

In this section, the experimental and simulation results are presented and compared. The compressive performance of the printed samples is summarized using stress-strain curves and histograms. Additionally, this section discusses the buckling performance incorporated with the simulation results.

### 3.1. Experimental compression testing

The stress-strain responses of various design parameters, including cross-section designs, patterns, and materials, are shown in Fig. 2. The experimental setup and the calculation of stress and strain can be found in Section 2.2. Three samples were tested for each design, with more information on the other two trials available in Supplementary Fig. S3. Initially, we observe that all designs sharing the same pattern exhibit almost identical Young's modulus values. Nevertheless, it is worth noting that all HEX cross-section designs consistently exhibit the highest yield strength. From Fig. 2, the CIR cross-section in PA12-Pattern C

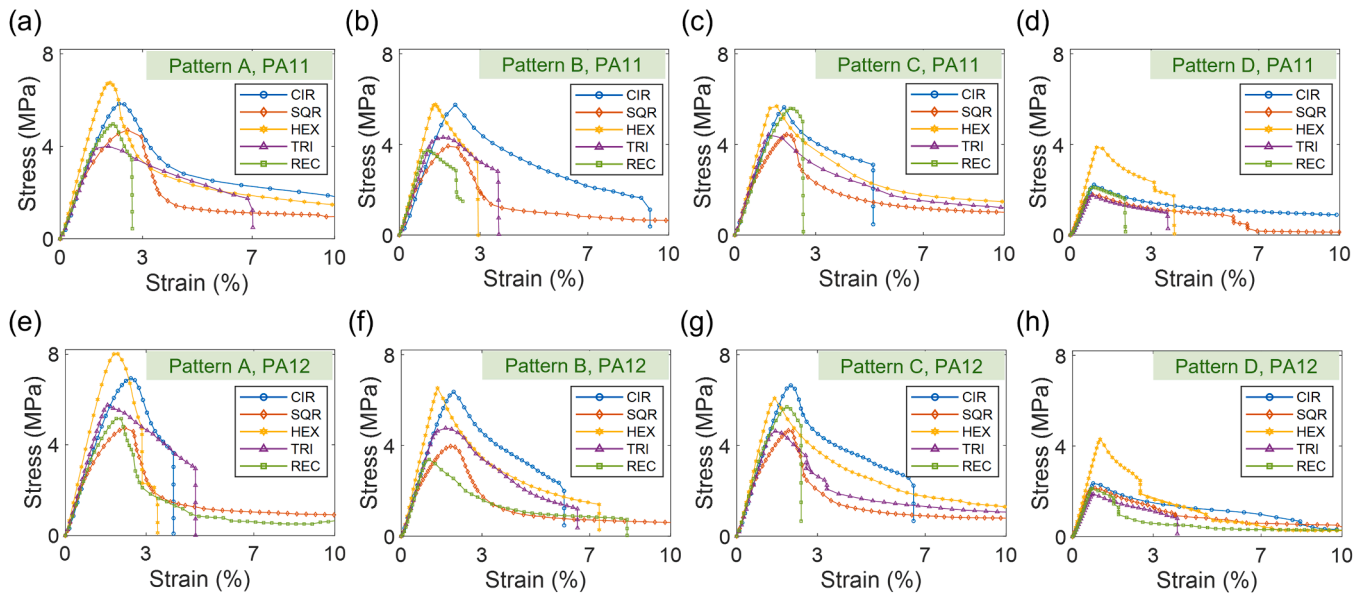


Fig. 2. Experimental stress-strain curves for experimentally tested samples of each design including varying cross-section, pattern, and material. (a)-(d) for PA11 and (e)-(h) for PA12.

demonstrates a higher yield strength than the HEX cross-section design. Despite this, the HEX cross-section has a higher yield strength on average compared to the CIR cross-section. This demonstrates that in the elastic regime, the HEX cross-section design has the best properties compared to other designs because it has the highest yield strength without sacrificing the modulus of elasticity. The reasoning and mechanism of this result is discussed in Section 3.2.

Other than cross-section effect, the influence of patterns (described in Section 2.1) is also studied. The results indicate that Pattern D has a substantially lower buckling strength compared to others, suggesting that the diagonal strut, creating multiple triangular structures, can greatly enhance the mechanical strength of the specimen through stabilization. Within different diagonal reinforced patterns, Pattern B and Pattern C, both containing the same cross-braced structures, have a very

similar stress-strain curve where their yield strength are both around 6.5 MPa with a yield strain of 1.5 - 2 %. Pattern A with HEX cross-section has the highest ultimate tensile strength, which is particularly interesting since this design has inherited the strengths of both the sea glass sponge and honeycomb structure.

While our initial findings are specific to PA12, we expand our investigation to evaluate the applicability of these results to an alternative polymer, PA11. An identical set of designs and experimental conditions is applied to the 3D printed specimens fabricated using PA11. The overarching trends observed in these tests remained consistent across all design variations, implying that the remarkable mechanical properties identified in the bio-inspired designs are likely attributable to the orientation of the struts rather than being primarily influenced by material properties. This is an important finding because it means that

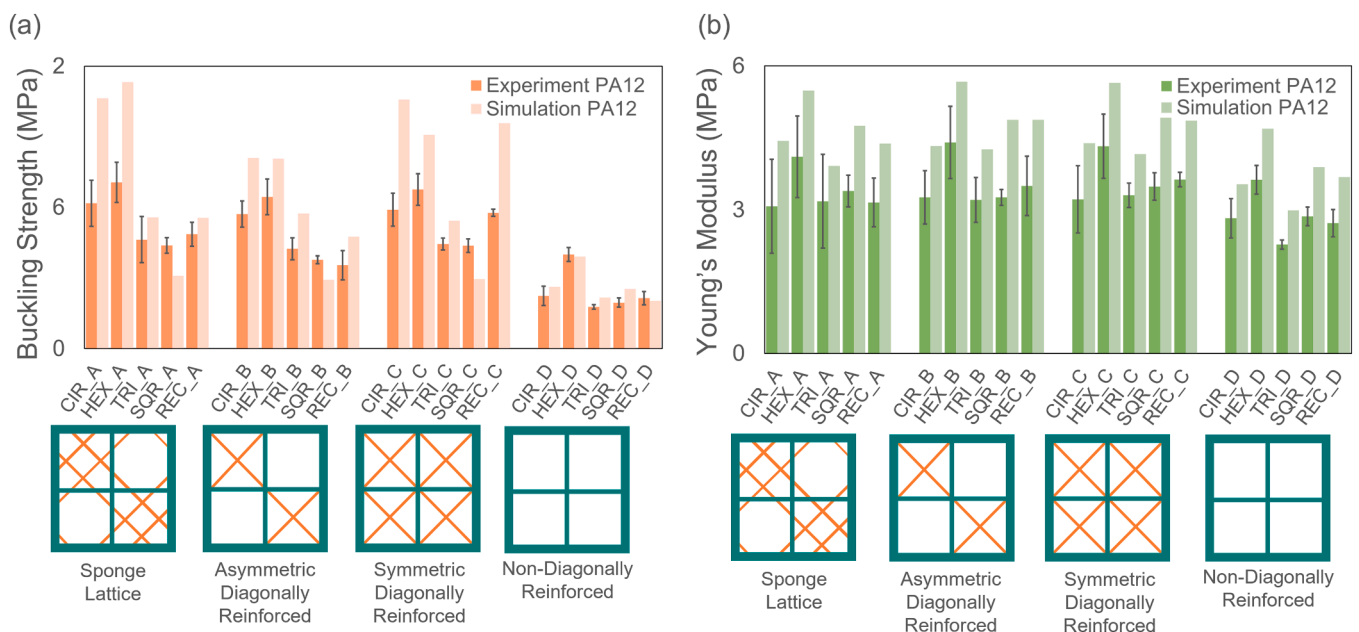


Fig. 3. Mechanical properties from PA12 experimental and simulated result for (a) buckling strength. (b) Young's modulus. The error bar shows the experimental variation between each trial.

the performance of the geometry is not significantly affected by variations in the properties of the MJF-printed polyamide group and may potentially be transferrable to other materials as well.

### 3.2. Comparison with simulation results

A comparative analysis is conducted between experimental measurements and simulation results, with a particular focus on two key mechanical properties: Young's modulus and buckling strengths, as summarized in Fig. 3a and b, respectively. Fig. 3 illustrates a comprehensive comparison of mechanical properties for PA12, encompassing both experimental and simulated results. Subfigure (a) provides insights into buckling strength, while Subfigure (b) examines Young's modulus. While the experiment shows its effective reinforcement capability, the diagonal strut introduces a level of complexity that challenges the accuracy of the simulation's prediction of mechanical performance. As shown in the histogram of Fig. 3a, the predicted buckling strength for Pattern D is all within the experimental range. Overall, the trends show a reasonable agreement between simulation and experimentation. However, the mechanical properties of the diagonal structure designs tend to be overestimated due to various factors. Some printing defects are observed and summarized in supplementary Fig. S4. We believe that one such factor is the reduction in sample dimensions that can occur during the printing and cooling process. Additionally, powder bed printing can result in void spaces and trapped unfused powder within the solid elements of the printed samples [65]. Furthermore, printing slanted components like diagonal structures can introduce more challenges to achieving accurate prints, leading to differences between experimental and simulation results.

The simulation and experimental results point to Pattern A with HEX cross-section to have the highest buckling strength. This is an interesting finding because it is reminiscent of the sea glass sponge structure that

has an improved ability to maintain its shape and stability when subjected to sudden changes in the shape of a structural component under compressive loading, especially when it is used in conjunction with the HEX cross-section. This is due to the way that the sea glass sponge system can distribute the load evenly throughout its structure by reinforcing not only the edge of the unit cell but also the side of the unit cell. The HEX cross-section adds additional strength and stability to the structure, further enhancing its ability to resist sudden changes in shape.

Drawing upon the earlier discussion, it becomes evident that the sea glass sponge's load distribution strategy and the incorporation of a HEX cross-section contribute significantly to structural strength. As mentioned earlier, all the designs that were tested had a very similar Young's modulus value. However, the top three designs have two things in common. First, they all have the HEX cross-section. Second, they all have diagonal struts to strengthen the unit cell. These diagonal struts are mostly at a 45-degree angle which divides the unit cell (square shape) into multiple isosceles triangles and reinforces the unit cell. Another geometrical parameter that can explain this mechanism is the node-to-node length. The diagonal struts not only create isosceles triangles but also create a lot of nodes (intersection of beams). These nodes can distribute load making the structure harder to fail. Also, the shorter the node-to-node length, the smaller the slenderness ratio, and the better the buckling resistance. This suggests that the use of diagonal struts in the design of the HEX cross-section may be particularly effective at increasing its elastic performance. It is of note the large standard deviation in the experimental data in regard to the Young's modulus data, highlighting the variation seen in the results. Further investigation reveals that these variations can be attributed to the prevalent porosity and layering effects in power bed fusion printing. Therefore, to enhance the precision of simulation models, it is necessary to acquire additional material characterization data across a range of print parameters and conduct micromechanical modeling to gain a deeper understanding of

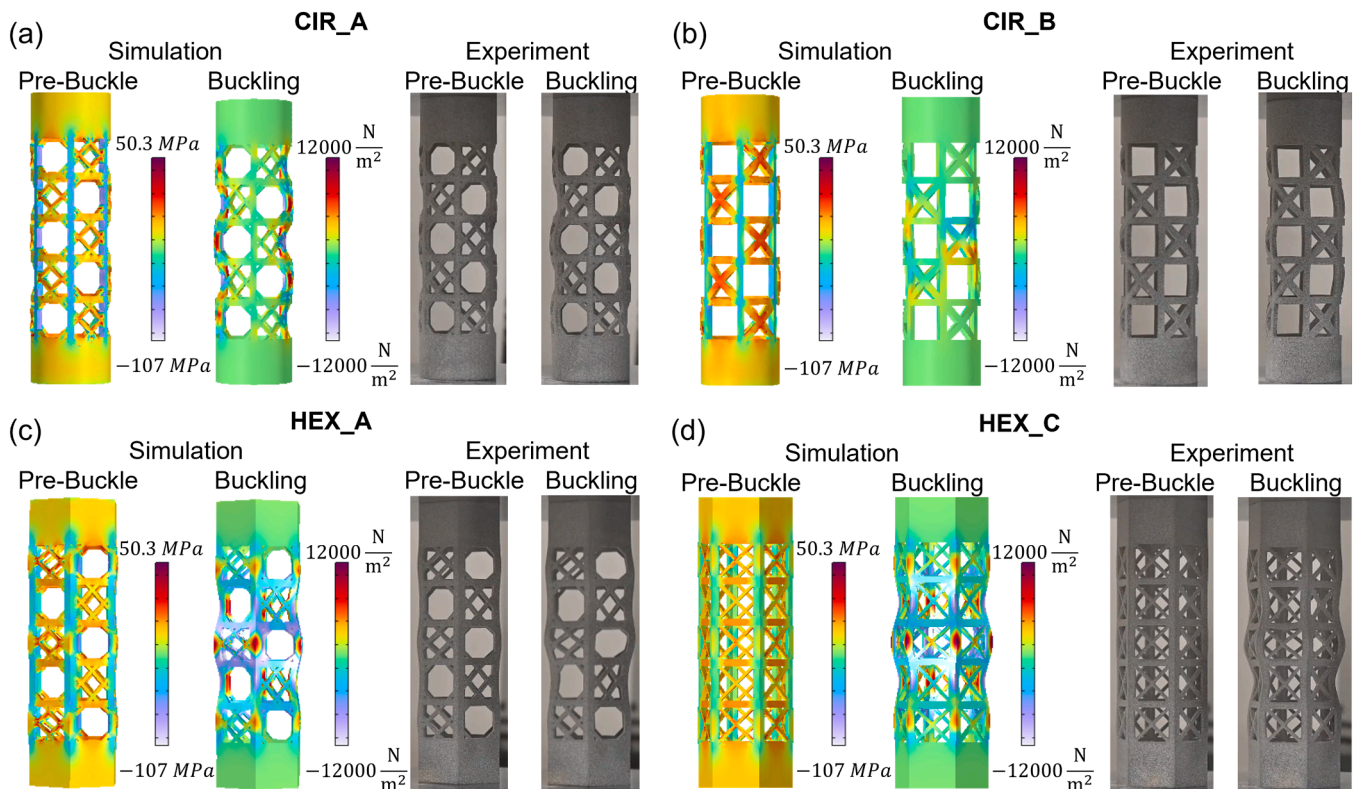


**Fig. 4.** Experimental and simulation results of four representative designs. The pre-buckle static simulation(left) shows the stress distribution of the design at true scale. Buckling simulation(right) presented the stress distribution of the design with a scale factor of 103 % of the maximum relative deformation field for better visualization. (a) circular cross-section with pattern A. (b) circular cross-section with pattern B. (c) hexagonal cross-section with pattern A. (d) hexagonal cross-section with pattern C.

these influences.

To further investigate the deformation modes of different designs, Fig. 4 shows the distribution of stress in the y-direction  $S_{yy}$  for four representative designs along with experimental results from compression testing (deformation snapshots for all other samples and materials can be found in Supplementary Fig. S5). The simulations incorporate geometric nonlinearity to ensure accurate comparisons with the experimental observations. The applied displacement in each simulation corresponds to the strain at the individual buckling strength observed in the experiments. Specifically, the applied displacement (both static and buckling simulation) is 2.4 % for CIR\_A, 1.9 % for CIR\_B, 1.9 % for HEX\_A, and 1.4 % for HEX\_C. In all cases, static simulations effectively represent structural deformation prior to buckling. During this initial deformation phase, structures exhibit continuous deformation with uniformly distributed stresses. Experimental observations align with simulations, displaying analogous deformation patterns and failure modes. Notably, the pre-buckling static simulation's stress fields reveal higher stress tensor values in the frame's vertical components due to their perpendicular alignment with the loading direction. Specifically, as depicted in Fig. 4a and c, CIR\_A's vertical components experience higher stress (ranging from blue to purple) compared to those in HEX\_A (ranging from green to blue), elucidating the higher Young's modulus of the HEX cross-section relative to the CIR cross-section. As the deformation progresses, the structures transition into the buckling stage, characterized by nonuniform deformations and localized buckling. The buckling simulations provide a more accurate representation of the stress distribution during this stage, capturing the shift from uniform to nonuniform deformation patterns. In particular, the buckling modes observed in the simulations closely match the experimental results, validating the accuracy of the computational models and capturing the primary failure mechanism of the structures. The concentration of high-stress regions at the center of the structures, away from the boundaries, suggests that the central sections are the most vulnerable to buckling. This out-of-plane buckling of the diagonal struts is a critical failure mode that directly impacts the overall structural integrity. Additionally, the CIR\_A and HEX\_A designs exhibit multiple high-stress regions distributed evenly along the structure during buckling, indicating a more effective load-bearing capacity. This combination of high tension and compression stress suggests that the sea glass sponge-inspired design enhances the frame's resistance to buckling by engaging more material

in resisting deformation. To further support these findings, a theoretical analysis using the Maxwell criteria and Euler buckling theory, presented in the supplementary information Note 1, shows that the sponge design is bending-dominated, with a critical buckling load more than six times higher than other designs, leading to excellent resistance to buckling. Literature has also presented theoretical models for analyzing thin-walled structures with different cross sections [67–69]. Ultimately, this novel design approach not only improves stiffness but also significantly delays the onset of catastrophic failure, making it a promising candidate for advanced structural applications.

### 3.3. Elastic energy absorption from experiments

Other than Young's modulus and buckling strength, the modulus of resilience is another important property that indicates a design's ability to store and release energy without undergoing permanent deformation. This measure reflects the quantity of elastic strain energy that the design can absorb before it begins to yield. A design with a high modulus of resilience ensures durability and longevity by preventing lasting changes to its structure within the elastic region. This leads to better functional efficiency and enhanced safety across a spectrum of uses, where resistance to deformation and shock absorption are critical. The calculation of modulus of resilience is detailed in Section 2.2, where the results of all design are summarized in Fig. 5. Designs printed using PA11 are plotted in Fig. 5a, while those printed using PA12 are plotted in Fig. 5b. Similar to Fig. 3, both histograms in Fig. 5 are organized based on their unit cell pattern. Each group comprises all five cross-sectional shapes indicated by the first three letters in the label.

When printed with PA11, the CIR\_A design exhibits the highest modulus of resilience ( $6.8 \times 10^6 \frac{J}{m^3}$ ), followed closely by HEX\_A ( $6.5 \times 10^6 \frac{J}{m^3}$ ). The CIR\_B, CIR\_C, and REC\_C designs have moderate resilience values ranging between  $5 - 6 \times 10^6 \frac{J}{m^3}$ . Among the various patterns, those with a circular cross-section demonstrate superior elastic energy absorption compared to other cross-sectional shapes. The high modulus of resilience observed in the CIR designs is attributed to their high strain values. This advantage comes from the geometric stability of the circular shape, which distributes stress more uniformly than shapes with corners. As a result, the level of buckling is more consistent locally, leading to uniform recovery from larger deformations. When evaluating different

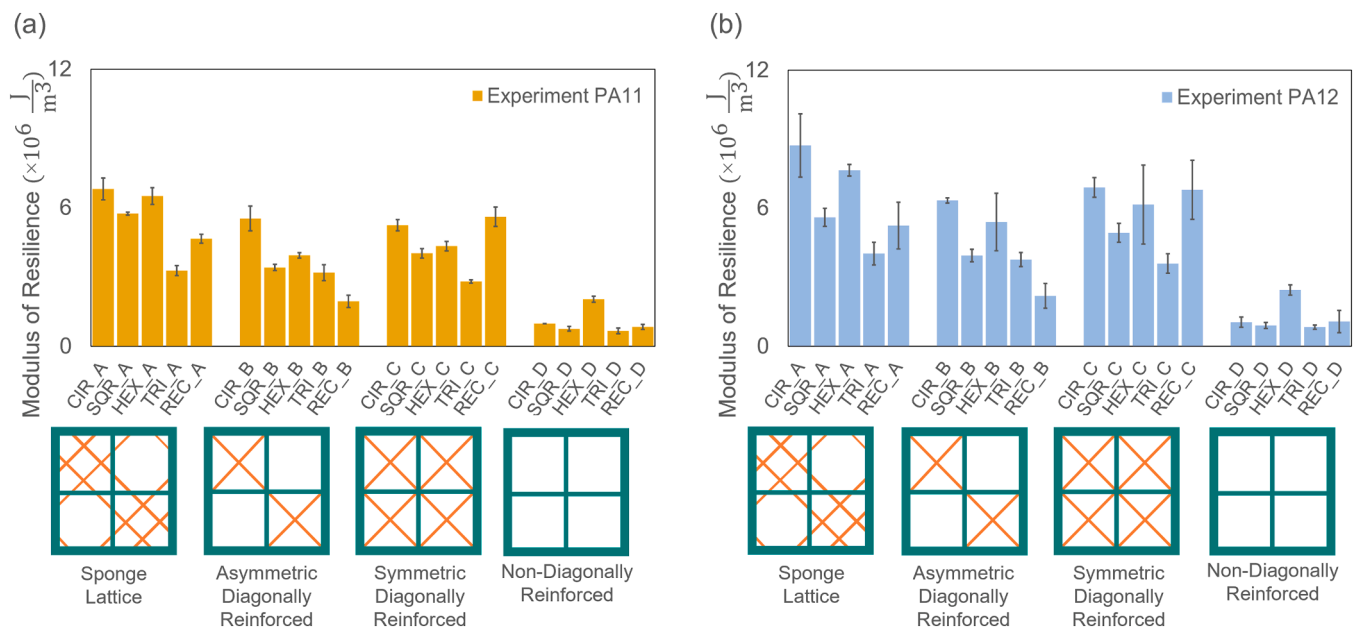


Fig. 5. Elastic strain energy absorption in the elastic region from experimental result for (a) material PA11. (b) material PA12. The error bar shows the experimental variation between each trial.

unit cell patterns, it is evident that the non-diagonally reinforced design has the lowest modulus of resilience, emphasizing the important role of diagonal reinforcements in enhancing mechanical performance under compression. Notably, pattern A consistently achieves the highest modulus of resilience compared to other patterns across all cross-sectional shapes, indicating the exceptional energy absorption capability of the sea sponge-inspired design. Similar trends are observed in PA12 printed samples, where CIR\_A again demonstrates the highest modulus of resilience. This consistency suggests that these beneficial properties are not significantly affected by variations in material within the same family, despite differences in material ductility. Overall, the sea sponge-inspired design with a circular cross-section proves to be the most effective in energy absorption, striking an excellent balance between high strength and ductility.

### 3.4. Stress field predictions from simulations

To provide a representative example when comparing designs, the von Mises stress field for the HEX\_A design and TRI\_A design is depicted in Fig. 6a and b. These simulations highlight the impact of cross-sectional geometry on stress distribution. Since forces are usually concentrated at the corner, the less sharp the corner is, the more uniform the stress distribution like the HEX cross-section. Therefore, the corner region of the cross-section view will exhibit the highest stress concentration. This is evident when analyzing the stress field predicted from our simulations, as well as through visual inspection of the cross-section diagrams. The color bar that represents the stress intensity clearly shows that the TRI cross-section design has more stress concentrated (70 MPa) at the corner or turning point, as compared to the HEX design shows a more uniform stress distribution with lower stress concentration (62 MPa). The main reason for this is that the TRI cross-section design has acute angles, which are sharper and more prone to stress concentration, as opposed to obtuse angles which enable a more effective stress distribution. These simulation results elucidate the mechanism behind the higher buckling strength observed in the HEX design, supporting that geometry plays a critical role in structural performance.

## 4. Conclusions

This research explores the compressive properties of sponge-inspired tubular lattices, building on the advantages of sponge-like patterns, such as their high strength-to-weight ratio, flexibility, and aerodynamic efficiency. By comparing five cross-sectional shapes and two polymer types for the tubular lattice design, alongside four different unit cell patterns, the impact of these parameters on structural performance was examined using both experimental and numerical methods. From the experiment and simulation analysis, the unit cell pattern and cross-sectional shape are critical influences on the mechanical behaviors of the tubular lattice, while the material type plays a minimal role within the polyamide group. All designs with diagonal strut reinforcement (Patterns A-C) exhibited an increase in Young's modulus, buckling strength, and modulus of resilience compared to Pattern D, attributed to the enhanced load distribution provided by the diagonal struts. The geometric properties of circular and hexagonal shapes provide lattices with greater structural integrity and reduced stress concentration, leading to improved mechanical properties. Among these, HEX\_A, based on a honeycomb shape and sea sponge pattern, showed improved buckling strength due to decreased node-to-node length, increased strut intersections, and reduced sharp corners. Additionally, Pattern A demonstrated the highest modulus of resilience among the unit cell patterns, with Pattern A featuring a circular cross-section showing the best elastic energy absorption, followed by the hexagonal cross-section. This study underscores the significant influence of cross-sectional shape and unit cell patterns on tubular lattice compressive properties, suggesting that designs inspired by sea glass sponges with honeycombs offer superior strength and buckling resistance, and with circular cross-

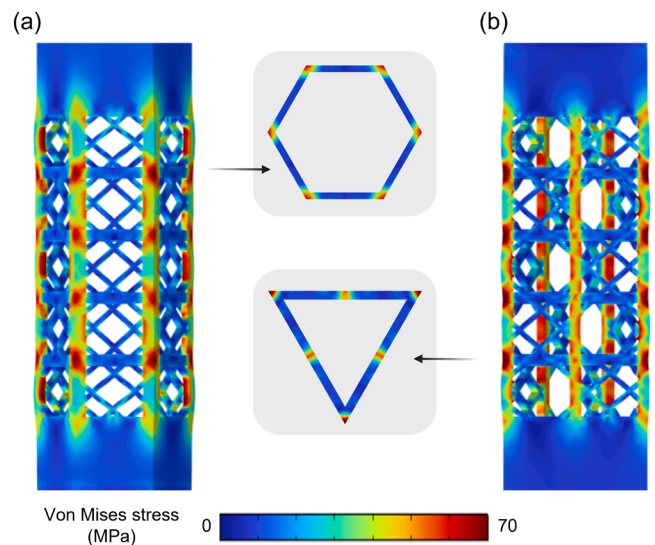


**Fig. 6.** Von mises stress field comparison between (a) HEX\_A and (b) TRI\_A design. The cross-section images (middle column with grey background) are taken from the same distance away from the top of each design.

section will have better elastic energy absorption. These findings are valuable for applications in aerospace, construction, automotive, and marine industries. Future research could optimize geometric parameters such as the radius-to-height ratio and unit cell size, further enriching our understanding and application of lattice structures.

### CRediT authorship contribution statement

**Ailin Chen:** Writing – original draft, Validation, Methodology, Investigation, Formal analysis. **Ukamaka Ezimora:** Writing – review & editing, Visualization, Methodology, Investigation. **Sangryun Lee:** Writing – review & editing, Methodology, Investigation, Formal analysis. **Jeong-Ho Lee:** Writing – review & editing, Investigation, Formal analysis. **Grace X. Gu:** Writing – review & editing, Methodology, Investigation, Conceptualization.

### Declaration of competing interest

The authors declare that they have no known competing financial interests or personal relationships that could have appeared to influence the work reported in this paper.

### Acknowledgements

We would like to acknowledge support from the 3D & Digital Manufacturing Lab of HP Labs, Office of Naval Research (Fund Number: N00014-21-1-2604), Army Research Office (Fund Number: W911NF2420036), and Savio computational cluster resource provided by the Berkeley Research Computing program.

### Supplementary materials

Supplementary material associated with this article can be found, in the online version, at [doi:10.1016/j.ijmecsci.2024.109815](https://doi.org/10.1016/j.ijmecsci.2024.109815).

### Data availability

All data supporting this study are included within the main paper and supplementary information.

## References

- [1] Meyers MA, et al. Biological materials: structure and mechanical properties. *Prog Mater Sci* 2008;53(1):1–206.
- [2] Barthelat F, Yin Z, Buehler MJ. Structure and mechanics of interfaces in biological materials. *Nature Rev Mater* 2016;1(4):1–16.
- [3] Naleway SE, et al. Structural design elements in biological materials: application to bioinspiration. *Adv Mater* 2015;27(37):5455–76.
- [4] Siddique SH, et al. Lessons from nature: 3D printed bio-inspired porous structures for impact energy absorption—a review. *Addit Manuf* 2022;58:103051.
- [5] Chen A, et al. Modeling bioinspired fish scale designs via a geometric and numerical approach. *Materials (Basel)* 2021;14(18):5378.
- [6] Chen P-Y, et al. Predation versus protection: fish teeth and scales evaluated by nanoindentation. *J Mater Res* 2012;27(1):100–12.
- [7] Habibi MK, et al. Viscoelastic damping behavior of structural bamboo material and its microstructural origins. *Mech Mater* 2016;97:184–98.
- [8] Zhang W, Xu J, Yu T. Dynamic behaviors of bio-inspired structures: design, mechanisms, and models. *Eng Struct* 2022;265:114490.
- [9] Ghimire A, et al. Tunable interface hardening: designing tough bio-inspired composites through 3D printing, testing, and computational validation. *Composites Part B: Eng* 2021;215:108754.
- [10] Lee S, et al. The origin of high-velocity impact response and damage mechanisms for bioinspired composites. *Cell Rep Phys Sci* 2022;12(2):3.
- [11] Wei Z, et al. Towards silent and efficient flight by combining bioinspired owl feather serrations with cicada wing geometry. *Nat Commun* 2024;15(1):4337.
- [12] Li L, et al. Optimization design of lightweight structure inspired by glass sponges (Porifera, Hexacnillida) and its mechanical properties. *Bioinspir Biomim* 2020;15(3):036006.
- [13] Wu J, et al. Multi-feature bionic gradient hierarchical lattice metamaterials with multi-synergistic crushing mechanisms. *Int J Mech Sci* 2024:109383.
- [14] Sharma D, Hiremath SS. Experimental and FEM study on the in-plane and out-plane loaded reversible dual-material bio-inspired lattice structures with improved energy absorption performance. *Compos Struct* 2023;303:116353.
- [15] Li Q-W, Sun B-H. Optimization of a lattice structure inspired by glass sponge. *Bioinspir Biomim* 2022;18(1):016005.
- [16] Arasuna A, et al. Structural characterization of the body frame and spicules of a glass sponge. *Minerals* 2018;8(3):88.
- [17] Walter S, Flinn B, Mayer G. Mechanisms of toughening of a natural rigid composite. *Mater Sci Eng: C* 2007;27(3):570–4.
- [18] Vangelatos Z, Yildizdag ME, Grigoropoulos CP. A designer's challenge: unraveling the architected structure of deep sea sponges for lattice mechanical metamaterials. *Extreme Mech Lett* 2023;61:102013.
- [19] Zhang Z, et al. Exploring tunable torsional mechanical properties of 3D-Printed tubular metamaterials. *Adv Eng Mater* 2024;26(9):2301876.
- [20] Du Z, et al. Artificial intelligence-enhanced bioinspiration: design of optimized mechanical lattices beyond deep-sea sponges. *Extreme Mech Lett* 2023;62:102033.
- [21] Aizenberg J, et al. Skeleton of Euplectella sp.: structural hierarchy from the nanoscale to the macroscale. *Science* 2005;309(5732):275–8.
- [22] Woesz A, et al. Micromechanical properties of biological silica in skeletons of deep-sea sponges. *J Mater Res* 2006;21(8):2068–78.
- [23] Ehrlich H, et al. Calcite reinforced silica–silica joints in the biocomposite skeleton of deep-sea glass sponges. *Adv Funct Mater* 2011;21(18):3473–81.
- [24] Robson Brown K, Bacheva D, Trask R. The structural efficiency of the sea sponge Euplectella aspergillum skeleton: bio-inspiration for 3D printed architectures. *J R Soc Interface* 2019;16(154):20180965.
- [25] Tavangarian F, Sadeghzade S, Davami K. A novel biomimetic design inspired by nested cylindrical structures of spicules. *J Alloys Compd* 2021;864:158197.
- [26] Weaver JC, et al. Hierarchical assembly of the siliceous skeletal lattice of the hexactinellid sponge Euplectella aspergillum. *J. Struct. Biol.* 2007;158(1):93–106.
- [27] Yang Z, et al. 3D printing of sponge spicules-inspired flexible bioceramic-based scaffolds. *Biofabrication* 2022;14(3):035009.
- [28] Johnson M, et al. Influence of moisture on the mechanical behavior of a natural composite. *Acta Biomater* 2010;6(6):2181–8.
- [29] Mayer G. New toughening concepts for ceramic composites from rigid natural materials. *J Mech Behav Biomed Mater* 2011;4(5):670–81.
- [30] Sharma D, Hiremath SS. In-plane elastic properties of the Euplectella aspergillum inspired lattice structures: analytic modelling, finite element modelling and experimental validation. *Structures*. Elsevier; 2023.
- [31] Zhang H, et al. In-plane crushing behavior and energy absorption of sponge-inspired lattice structures. *Int J Mech Sci* 2024;274:109328.
- [32] Sharma D, Hiremath SS. Bio-inspired repeatable lattice structures for energy absorption: experimental and finite element study. *Compos Struct* 2022;283:115102.
- [33] Fernandes MC, et al. Mechanically robust lattices inspired by deep-sea glass sponges. *Nat Mater* 2021;20(2):237–41.
- [34] Li Y, Hu D, Yang Z. Crashworthiness design of a sponge-inspired multicell tube under axial crushing. *Int J Mech Sci* 2023;244:108070.
- [35] Wang P, et al. Bio-inspired multi-cell tubular structures approaching ideal energy absorption performance. *Mater Des* 2023;225:111495.
- [36] Fernandes MC, et al. Mechanical and hydrodynamic analyses of helical strake-like ridges in a glass sponge. *J R Soc Interface* 2021;18(182):20210559.
- [37] Faluccci G, et al. Extreme flow simulations reveal skeletal adaptations of deep-sea sponges. *Nature* 2021;595(7868):537–41.
- [38] Chen HS, Jia Z, Li L. Lightweight lattice-based skeleton of the sponge On the multifunctional design. *J Mech Behav Biomed Mater* 2022:135.
- [39] Kulchin YN, et al. Optical and nonlinear optical properties of sea glass sponge spicules. *Biosilica in Evol Morphogenesis Nanobiotechnol: Case Study Lake Baikal* 2009:315–40.
- [40] Sarikaya M, et al. Biomimetic model of a sponge-spicular optical fiber—mechanical properties and structure. *J Mater Res* 2001;16(5):1420–8.
- [41] Luo R, et al. Super durable graphene aerogel inspired by deep-sea glass sponge skeleton. *Carbon N Y* 2022;191:153–63.
- [42] Wang P, et al. Bio-inspired vertex modified lattice with enhanced mechanical properties. *Int J Mech Sci* 2023;244:108081.
- [43] Mistry Y, et al. Bio-inspired selective nodal decoupling for ultra-compliant interwoven lattices. *Commun Mater* 2023;4(1):35.
- [44] Yan J, et al. A wide-range stiffness-tunable soft actuator inspired by deep-sea glass sponges. *Soft Robot* 2022;9(3):625–37.
- [45] Liu Q, et al. 3D printable strong and tough composite organo-hydrogels inspired by natural hierarchical composite design principles. *Nat Commun* 2024;15(1):3237.
- [46] Wei K, et al. Lightweight composite lattice cylindrical shells with novel character of tailorable thermal expansion. *Int J Mech Sci* 2018;137:77–85.
- [47] Li WW, et al. A more weight-efficient hierarchical hexagonal multi-cell tubular absorber. *Int J Mech Sci* 2018;140:241–9.
- [48] Liu Q, et al. Crash responses under multiple impacts and residual properties of CFRP and aluminum tubes. *Compos Struct* 2018;194:87–103.
- [49] Montazeri A, et al. 3D-printed twisting tubular metamaterials with tunable mechanical and torsional characteristics. *Int J Mech Sci* 2024:262.
- [50] Wang ZG, et al. On the crashworthiness of bio-inspired hexagonal prismatic tubes under axial compression. *Int J Mech Sci* 2020:186.
- [51] Azimi MB, Asgari M. Energy absorption characteristics and a meta-model of miniature frusta under axial impact. *Int J Crashworthiness* 2016;21(3):222–30.
- [52] Sharma D, Hiremath SS. Compressive fatigue response of Al-Si10-Mg bionic thin tubes under constant and variable amplitude loading. *Int J Fatigue* 2023:168.
- [53] Sharma D, Hiremath SS, Kenchappa NB. Effect of heat treatment on the variable amplitude fatigue life and microstructure of the novel bioinspired Ti-6Al-4V thin tubes fabricated using Selective Laser Melting process. *Fatigue Fract Eng Mater Struct* 2023;46(3):975–86.
- [54] Sharma D, Hiremath SS. Design of Euplectella aspergillum based bionic thin tubes for impact absorbing application under different loading conditions. *J Mater Res Technol-Jmr&T* 2023;23:3790–810.
- [55] Zhang Z, et al. Unveiling the mechanics of deep-sea sponge-inspired tubular metamaterials: exploring bending, radial, and axial mechanical behavior. *Thin-Walled Struct* 2024;196:111476.
- [56] Niu J, et al. Influence of cross-sectional shape on the mechanical properties of concrete canvas and CFRP-reinforced columns. *Adv Mater Sci Eng* 2021:1–14.
- [57] Ayough P, et al. The effects of cross-sectional shapes on the axial performance of concrete-filled steel tube columns. *J Constr Steel Res* 2021;176:106424.
- [58] Soleimani F, Mangalathu S, DesRoches R. A comparative analytical study on the fragility assessment of box-girder bridges with various column shapes. *Eng Struct* 2017;153:460–78.
- [59] Assaee H, et al. Axial splitting of composite columns with different cross sections. *Thin-Walled Struct* 2016;99:109–18.
- [60] Qiu X, Zhang J, Yu T. Collapse of periodic planar lattices under uniaxial compression, part II: dynamic crushing based on finite element simulation. *Int J Impact Eng* 2009;36(10–11):1231–41.
- [61] Fernandes, M.C., et al., **Supplementary information: mechanically robust lattices inspired by deep-sea glass sponges.**
- [62] Badini C, Padovano E. Powder Bed Fusion. High resolution manufacturing from 2D to 3D/4D printing: applications in engineering and medicine. Springer; 2022. p. 81–103.
- [63] Pandelidi C, Lee KPM, Kajtaz M. Effects of polyamide-11 powder refresh ratios in multi-jet fusion: a comparison of new and used powder. *Addit Manuf* 2021;40:101933.
- [64] Mahmoud M, Huitorel B, Fall A. Rheology and agglomeration behavior of semi-crystalline polyamide powders for selective laser sintering: a comparative study of PA11 and PA12 formulations. *Powder Technol* 2024;433:119279.
- [65] Chen AY, et al. Effect of build parameters on the mechanical behavior of polymeric materials produced by Multijet fusion. *Adv Eng Mater* 2022;24(9):2100974.
- [66] Chen A, et al. Multi Jet Fusion printed lattice materials: characterization and prediction of mechanical performance. *Mater Adv* 2023.
- [67] Wierzbicki T, Abramowicz W. On the crushing mechanics of thin-walled structures. *J Appl Mech-Trans Asme* 1983;50(4a):727–34.
- [68] Abramowicz W, Wierzbicki T. Axial crushing of multicorner sheet metal columns. *J Appl Mech-Trans Asme* 1989;56(1):113–20.
- [69] Liu Y, Day ML. Development of simplified thin-walled beam models for crashworthiness analyses. *Int J Crashworthiness* 2007;12(6):597–608.